Vortex Flow on a Hypersonic Spaceplane Configuration

U.Herrmann
DLR, Institute of Design Aerodynamics
Lilienthalplatz, 38108 Braunschweig, Germany

Abstract

The flow around the forebody of a generic spaceplane configuration is investigated. A conical upwind Euler method is used to calculate aerodynamic forces and flow structures of the delta wing geometry with blunted leading edges. The leeside flow structure at hypersonic Mach numbers of 4 and 6 is studied. Two types of shock-induced vortical flows are found at high angles of attack for both Mach numbers. The influence of discretization errors on the calculated conical leeside flow structures are addressed. The inviscid flow is compared to 3D Navier-Stokes solutions. The limits of conical Euler methods as fast design tools are discussed.

1.Introduction

Future hypersonic cruise configurations have to meet both, excellent high and low speed aerodynamic performance. These requirements and the demand for large fuel volumes and a heat protection system drive the spaceplane's planform and cross sectional design. Blended body double delta wing configurations are expected to meet the aerodynamic and volumetric requests. Such double delta geometries generate additional vortex lift on their leeside at high angles of attack. That improves the configuration's aerodynamic performance. The forebody's pressure side is shaped to maximize the precompression of the engine's input mass flow. Temperature boundaries of the materials determine the amount of body nose and wing leading edge bluntness for hypersonic flight conditions. Flight mechanical characteristics and the engine integration pose additional constraints for the design.

Because of the multifold constraints and the required high aerodynamic performance at different speed regimes spaceplanes are difficult multipoint designs. Fast and accurate numerical tools capable of estimating aerodynamic performance and associated flow structures are therefore necessary. Modern materials enable the design of relativly sharp geometries. Spaceplane forebodies which consists of delta wings blended with a body have relativ small nose radii. They can be approximated as pointed conical thick delta wings. For pointed forebody geometries conical Euler methods seem to be adequate numerical tools considering the tradeoff between accuracy and numerical effort.

A generic spaceplane design for cruise at M_∞=4 is shown in **Fig. 1**. The configuration consists of a double delta wing planform blended with a body.

The present paper adresses the flow structure of the forebody shape of Fig. 1 at two hypersonic Mach numbers. The calculated conical vortex flow is investigated and compared to 3D Navier-Stokes results. Limits of conical Euler methods are described to evaluate the applicability of these tools in designing hypersonic forebodies.

2.Governing Equations

The integral form of the three-dimensional Euler equations using nondimensional variables in a cartesian coordinate system can be written as

$$\frac{\partial}{\partial t}\int_V \vec{W}\,dv + \int_{\partial V} \bar{F}\cdot\hat{n}\,ds = 0 \qquad (1)$$

where

$$\vec{W} = [\rho, \rho u, \rho v, \rho w, \rho E]^T$$

is the vector of conserved quantities with ρ,u,v,w and E denoting density, cartesian velocity components and specific total energy, respectively. V denotes an arbitrary control volume fixed in time and space with boundary ∂V and the outer normal $\hat{n}$. The total enthalpy is given by

$$H = E + p/\rho \quad . \qquad (2)$$

The flux tensor $\bar{F}$ is given as

$$\hat{\bar{F}} = \begin{bmatrix} \rho u\hat{k}_x & +\rho v\hat{k}_y & +\rho w\hat{k}_z \\ (\rho u^2+p)\hat{k}_x & +\rho uv\hat{k}_y & +\rho uw\hat{k}_z \\ (\rho uv)\hat{k}_x & +(\rho v^2+p)\hat{k}_y & +\rho vw\hat{k}_z \\ (\rho uw)\hat{k}_x & +\rho vw\hat{k}_y & +(\rho w^2+p)\hat{k}_z \\ (\rho uE+up)\hat{k}_x & +(\rho vE+vp)\hat{k}_y & +(\rho wE+wp)\hat{k}_z \end{bmatrix}$$

where $\hat{k}_x$, $\hat{k}_y$, $\hat{k}_z$ denote the cartesian coordinate directions. Assuming that air behaves as a calorically perfect gas, the pressure is calculated by the equation of state

$$p = (\gamma - 1)\,\rho\,(E - \frac{u^2 + v^2 + w^2}{2}) \qquad (3)$$

where γ denotes the ratio of specific heats. The Navier-Stokes equations governing viscous flows may be found in textbooks.

3. Numerical method

3.1 Spatial Discretization

The numerical method solves the unsteady Euler equations in integral form. The approximation follows the method of lines which decouples the discretization in space and time. Using the finite volume approach, the approximation of the integral for a hexahedral control volume surrounding the grid node (i, j, k) (see **Fig. 2**) yields a system of ordinary differential equations with respect to time

$$V_{i,j,k} \cdot \frac{\partial}{\partial t} \vec{W}_{i,j,k} = -\vec{R}_{i,j,k} \quad . \qquad (4)$$

Here, $\vec{W}_{i,j,k} = [\rho, \rho u, \rho v, \rho w, \rho E]^T_{i,j,k}$ represents the conserved quantities at grid node (i, j, k), where ρ, u, v, w and E denote the density, Cartesian velocity components and total energy, respectively. $\vec{R}_{i,j,k}$ represents the net flux (residuum) of mass, momentum and energy over the control volume (i, j, k) with volume $V_{i,j,k}$. It is calculated as

$$\vec{R}_{i,j,k} = \vec{R}_{i+\frac{1}{2},j,k} - \vec{R}_{i-\frac{1}{2},j,k} + \vec{R}_{i,j+\frac{1}{2},k} - \vec{R}_{i,j-\frac{1}{2},k} + \vec{R}_{i,j,k+\frac{1}{2}} - \vec{R}_{i,j,k-\frac{1}{2}} , \qquad (5)$$

with $\vec{R}_{i+\frac{1}{2},j,k}$ denoting the flux through cell face $i+1/2$. In the following the flux vector splitting for the approximation of the convective flux is briefly described.

As shown in [1],[2] the discrete inviscid flux can be interpreted as a sum of a Mach number weighted average of the left (L) and right (R) state at the cell face $i+1/2$ (see Fig. 2) and a scalar dissipative term. It reads

$$\vec{R}_{i+\frac{1}{2},j,k} = |\vec{S}|_{i+\frac{1}{2},j,k} \left(\frac{1}{2} M_{i+\frac{1}{2},j,k} \left(\begin{bmatrix} \rho c \\ \rho cu \\ \rho cv \\ \rho cw \\ \rho cH \end{bmatrix}_L + \begin{bmatrix} \rho c \\ \rho cu \\ \rho cv \\ \rho cw \\ \rho cH \end{bmatrix}_R \right) - \frac{1}{2} \Phi_{i+\frac{1}{2},j,k} \left(\begin{bmatrix} \rho c \\ \rho cu \\ \rho cv \\ \rho cw \\ \rho cH \end{bmatrix}_R - \begin{bmatrix} \rho c \\ \rho cu \\ \rho cv \\ \rho cw \\ \rho cH \end{bmatrix}_L \right) \right) + \begin{bmatrix} 0 \\ s_x p \\ s_y p \\ s_z p \\ 0 \end{bmatrix}_{i+\frac{1}{2},j,k} \qquad (6)$$

where

$$\vec{S}_{i+\frac{1}{2},j,k} = [s_x, s_y, s_z]^T_{i+\frac{1}{2},j,k} \qquad (7)$$

denotes the surface vector normal to the cell face $i+1/2$. The quantities c, H and p represent the speed of sound, enthalpy and pressure, respectively. $M_{i+\frac{1}{2},j,k}$ denotes the advection Mach number at the cell face $i+1/2$ which is calculated according to [1] as

$$M_{i+\frac{1}{2},j,k} = M^p_L + M^m_R \qquad (8)$$

where the split Mach numbers $M^{p/m}$ are defined as polynomials of the left and right Mach numbers according to van Leer [3].

The pressure p at cell face $i+1/2$ is calculated in a similar way as

$$p_{i+\frac{1}{2},j,k} = p^p_L + p^m_L \qquad (9)$$

where $p^{p/m}$ denote the split pressure defined also by polynomials of the left and right Mach numbers [3]. As described in [2],[4] the definition of the factor ϕ determines the amount of numerical dissipation inherent in the discrete convective part of the flux vector. Moreover, the definitions of ϕ for the well-known van Leer flux vector split scheme and the AUSM scheme [1] with low numerical dissipation differ only by a Mach number scaled term. This fact allows easy implementation of a Navier-Stokes solver which uses van Leer's flux vector splitting at shocks and has low numerical diffusion in smooth

regions of the flow [4]. However, the inviscid flow solutions presented here are obtained with van Leer's scheme applied throughout the computational domain by which the robustness of the overall method is increased.

The spatial accuracy of the scheme depends on the determination of the left and right state at cell interface $i+1/2$. For a first-order scheme the flow quantities at the left and right state are given by their values at the neighboring mesh points i, j, k and i + 1, j, k, respectively (see Fig. 2). Higher order accuracy is obtained with the MUSCL approach which uses extrapolation of flow quantities for the calculation of the left and right state. The van Albada limiter function [5] is employed which switches the second-order accurate scheme to first order accuracy at shocks in order to guarantee shock capturing without spurious oscillations.

In supersonic flow around pointed, conical bodies flow variables are constant along rays which start at the apex of the body, i.e. the flow field itself is conical. In order to calculate such a flow field,a simplified finite discretization is used. The physical domain is now divided into special hexahedral cells, see **Fig. 3**. Due to the conical flowfield flow variables are constant at the edges of the front and rear face of the control volume wich are connected through one ray. Only one layer of cells between x_1 und x_2 is necessary for the determination of the whole conical flow field. Applying the discretized equations to this special control volume results in a kind of source term which represents the change of metric quantities in the axial coordinate direction. The solution scheme itself is unaffected. Note that only one mesh plane has to be discretized. This is the main effect which remarkably reduces the numerical effort of conical Euler schemes.

3.2 Time Integration

The spatial discretization results in a system of ordinary differential equations with respect to time. For the calculations the solution has been advanced in time employing an explicit three-stage scheme for the inviscid and an explicit five-stage scheme for the 3D Navier-Stokes calculations. Local time stepping and implicit residual smoothing have been applied to accelerate the convergence to the steady state. For the Navier-Stokes solutions a multigrid algorithm is applied in addition.

4.Results

4.1 The calculated conical flow structure at M_∞=4

The spaceplane planform is drawn on the right side of Fig. 1. The forebody part of the present work is shaded. On the figure's left side the mesh around the approximated geometry is shown. The forebody is approximated by a pointed conical delta wing having the displayed blended body wing cross-section and identical sweep angle as the shaded spaceplane forebody. Parts of the flowfield around the wing leading edge where highly accelerated flow is expected were carefully discretized as shown in **Fig. 4**. An elliptic mesh generation tool [6],[7] was used to create different fine meshes with 100x20, 200x40 and 400x80 cells.

The calculated conical flow structure on the medium (200x40 cells) mesh at M_∞=4 is depicted in **Fig. 5** using iso Mach lines in cross-sections. The three pictures at 5°, 7° and 10° angle of attack (increasing from top to bottom of this figure) show the outer bow shock as well as the mesh boundary on the picture's right side. The strength of the outer bow shock as well as the pressure on the delta wing's lower side increase with angle of attack. The growing pressure difference to the leeside accelerates the flow more and more around the blunt wing leading edge visualized through increased local Mach number. Crossflow velocities exist and rise in the expansion region. They are highest at the body and easily reach sonic speeds also for low angles of attack. At the symmetry plane they have to be zero.

Hence, there exists a crossflow shock which reduces the crossflow velocities and turns the flow direction from crossflow to axial flow. Its strength increases with angle of attack. The shock reaches further out into the field and moves simultaneously toward the symmetry plane for higher angles of attack. There is also shock strength variation normal to the body. Beeing strongest at the body the crossflow shock weakens with increasing body normal distance and vanishes where crossflow velocities are lower than sonic.

The shock strength variation normal to the body causes entropy gradients. They may generate vortices depending on the gradient's value. Here for α=10° a crossflow shock exists which terminates the outer expansion region. This shock is located more inboard than for α=5° and α=7°. However, more shocks exist in this solution. Close to the leading edge another crossflow shock is formed which generates an inviscid vortex. A third crossflow shock is formed between the vortex and the wing surface. The leeside vortex is flat and reaches over nearly 50% of the delta wing span. The vortex can be detected in Fig. 5 through two wall parallel Mach gradient belts.

In **Fig. 6** the flow structures for M_∞=4 and the three angles of attack of Fig. 5 are represented by pictures of conical streamlines. They are projections of 3D streamlines onto a sperical surface centered at the apex of the wing. Undisturbed free stream in conical solutions results in plots where streamlines start at the outer mesh boundary and run straight into the

mesh center. Here streamlines are plotted to visualize the calculated vortex shape in the high-angle-of-attack (α=10°) solution. The vortex is easier to detect than in the iso Mach line plot. An additional vortex developing further inboard on the horizontal body part is visible. The pictures for lower angle of attack show fully attached flow.

4.2 The calculated conical flow structure at M_∞=6

The higher onflow Mach number of 6 is choosen to investigate changes of the flow structure with Mach number. They are expected because the leading edge normal Mach number changes from subsonic at M_∞=4 to supersonic at M_∞=6. The same angles of attack as before were calculated on all three meshes.

The resulting flow structures are depicted using iso Mach lines in **Fig. 7**. The outer bow shock becomes stronger and moves toward the wing. The expansion regions is larger for all angles of attack. This is shown by the increased crossflow shock's extent into the fields. For α=5° and 7° attached solutions exist which have stronger crossflow shocks than in the lower Mach number solutions of Fig. 5. The increased onflow Mach number also moves the crossflow shocks more inboard. The α=10° solution shows a complicated shock structure of two crossflow shocks which seem to interact. A shock exists which is strongly curved near the wing surface. Behind this curved shock a separation bubble is generated. The bubble changes the pressure behind the shock and therefore the shock is located further to the wing leading edge than the shock in the α=7° solution. The second crossflow shock terminates the expansion region in the field. Caused by the shock interaction the strength of the second shock is reduced towards the wall. **Fig. 8** illustrates the calculated flow structures using conical streamlines. The two lower angle of attack solutions show attached flow. The differences in the streamline plots for attached flow between Fig. 6 and Fig. 8 are small. At α=10° both plots differ significantly. The large separation behind the shock at the wing leading edge in the lower Mach number solution changes here to a flat tiny separation bubble. The separation location moves significantly with the onflow Mach number change. An additional vortex forming on the upper body part near the symmetry plane is also visible.

The attached crossflow structures for both hypersonic onflow Mach numbers are similar. This is due to the fact that in both cases the bow shock is detached from the blunt leading edge. The detached bow shock yields flow expansion around the blunt subsonic leading edge as well as around the supersonic leading edge. The attached expansions are terminated by crossflow shocks.

For α=10° the separated flow structure changes with increasing onflow Mach number. Distinguishable vortex and shock topologies are calculated for the two Mach numbers despite similar detached bow shocks enabling for expanded flow around the blunt leading edge. For M_∞=4 this expansion is terminated by a strong crossflow shock close to the wing leading edge which creates a big separation. For the higher onflow Mach number the expansion is terminated further inboard by a shock which generates a separation bubble.

4.3 Shock-induced inviscid separations and numerical influence

The numerical accuracy of the attached flow solution at M_∞=4, α=5° is investigated first. **Fig. 9** shows plots of c_p over wing span for the three mesh densities. The solutions show excellent agreement. Crossflow shock strength and position is identical on all meshes. The corresponding convergence histories are given in **Fig. 10**. On all meshes nearly five orders of magnitude convergence (machine zero on 32 bit workstations) is reached after ~1600 time steps on the coarse mesh and 6000 time steps on the fine mesh. The calculated lift coefficients show almost no variation with mesh density. Fig. 9 and Fig. 10 confirm that grid converged and residual converged solutions were obtained for attached flow at M_∞=4.

At M_∞=6 comparable convergence rates and mesh converged solutions are obtained for attached flow. These plots are not repeated here.

The two conical shock-induced separations calculated for M_∞=4 and 6 show complete different convergence behaviour. This is highlighted in **Fig. 11**. The high-Mach-number solution reaches machine zero after ~2800 iterations while the solution at M_∞=4 does not converge to such low residual levels. It reaches a stable oscillating state after ~3000 iterations on the medium mesh at relativly high residual levels. The amplitude and wavelength of this oscillation depends on mesh density and is probably influenced by numerical errors. The convergence plots of the two remaining meshes (coarse and fine mesh) are not shown here because they show similar behaviour. Their solutions also oscillate between two extreme states after a residual drop of little more than two orders of magnitude.

The two extreme states of the oscillating solution on the fine mesh at M_∞=4; α=10° are discussed first. The calculated flow structure at the low and high residual points of the oscillation are shown by combining iso Mach lines and conical streamlines. Both, **Fig. 12** and **Fig. 13** show the same global and detailed views of the separated flow. The flow structure is characterized by three crossflow shocks. The first shock is lo-

cated close to the wing leading edge. It has the same location in both figures. The outer expansion region is terminated by a crossflow shock which does not reach the body surface. Under the flat primary vortex and perpendicular to the wall a third shock is found. At its foot the secondary counter-rotating separation starts. Comparing both pictures it is clear that the outer flow field seems stable and is only slightly influenced by the changing shapes of the vortices. The primary vortex oscillates between phases having one center (low residual level), Fig. 12 and two/three separate centers at higher residuals, Fig. 13. This behaviour is caused by the oscillating position and strength of the embedded third crossflow shock. The counter-rotating secondary separation is affected by the third shock's position and strength variation. The changing shape of the counter-rotating secondary vortex as well as its movement forces the two extreme states of the primary vortex. The low numerical dissipation of the fine mesh allows to calculate a more detailed but oscillating flow structure than on coarser meshes. It is supposed that lack of natural viscous damping is responsible for the oscillating crossflow shock and therefore changing shape of the secondary separation. This effect seems to prevent convergence to a steady state solution. It may also be possible that for this flow type no stable solution exists at all.

The plot of c_p over wing span, **Fig. 14** visualizes the separation locations of the M_∞=4 solutions. Only the part of the outer wing span is drawn. Additionally, the pressure distributions of the two extreme states of the oscillating fine-mesh solution are included. The shape of the blunt wing cross-section is also shown. Careful examination leads to the following observations. The calculated separation location on the coarse mesh is found at the most far out position. The flow does not expand as much as on the finer meshes before shock-induced separation occurs. The separation of the medium mesh solution is at y/s~0.99 and differs for one cell from the fine mesh solution. Therefore the separation location is mesh converged at that location. The c_p distributions of the two fine mesh and the medium mesh solutions show at different positions and with changing strength the embedded third crossflow shock. The 100x20 mesh is too coarse to resolve this detail. Therefore, all leeside pressure plots do not have much in common with each other except the shock generated primary separation at the wing leading edge.

Summarizing Fig. 14 shows that coarser mesh solutions result in separation locations closer to the wing tip. Increasing the mesh density enables to represent stronger expansions before separation takes place. Detailed flow structures are resolvable on finer meshes.

A different impression of the separation behaviour at M_∞=6; α=10° is shown in **Fig. 15** by c_p distributions over wing span. The cross-section geometry is drawn to get a better impression of the separation location. The pressure distributions calculated on all meshes only differ in the separated flow region. In this case identical expansion pressure levels are reached on all meshes. The crossflow shock location moves towards the leading edge with decreasing mesh density as could be observed in the M_∞=4; α=10° flow solutions for the same mesh densities. But the coarse mesh solution shows attached flow with a crossflow shock positioned further inboard than the other solutions.

Stable converged flow solutions were calculated for all M_∞=6 onflow conditions and all mesh densities. The following explanation seems reasonable and valid for the numerical influence on the observed separations for both Mach number cases:

Numerical flow calculations are always affected by numerical dissipation which depends on the formulation of the spacial discretization scheme and the mesh density involved. Upwind schemes as the one used here generate very low numerical dissipation. For all numerical schemes discretization errors grow with the cell size of the mesh. That means that coarser meshes generate higher levels of numerical dissipation because flow gradients resolved with less cells decrease. Flows investigated here generate numerical errors primarily in the expansion region where high flow gradients exist in wall-normal direction. These errors act in inviscid flow calculations like boundary layers in viscous flows. Found by [8],[9] and others it is repeated here that the primary source for inviscid separation is a sufficiently strong shock. But the numerical dissipation can influence the shock-induced separation depending on the dissipation level.

Influences of numerical dissipation on separated inviscid flow structures are found in the present results. Numerical dissipation may smear solution details depending on the dissipation level. Increased mesh-inherent numerical dissipation may prevent the calculation of flow details. This is true for both α=10° coarse mesh solutions. While the coarse M_∞=4 solution only resolves the primary vortex without details the higher numerical dissipation in the M_∞=6 solution prevents forming the separation bubble. Decreasing the numerical dissipation at the lower hypersonic onflow Mach number increases the solution detail richness. The finest mesh (lowest numerical dissipation) is able to resolve a shock-induced secondary separation while the next coarser mesh only calculates that shock without separation. At M_∞=6 the shape of the tiny separation bubble is affected by numerical

dissipation. As a consequence no fully mesh converged separation is calculated for this onflow conditions. Different local mesh densities near the leading edge (M_∞=4, mesh converged shock position with primary separation) and between y/s=0.6 ÷ 0.8 result in local variations of mesh-inherent dissipation. It is concluded that higher numerical dissipation in the crossflow shock region at M_∞=6 is the source of the changing shape of the separation bubble influencing the shock position. That prevents the calculation of a mesh converged shock position although the solutions are residual converged.

4.4 Comparison of flow structures calculated with a conical Euler- and a Navier-Stokes method

Separated conical flow structures are compared to flow solutions obtained with a 3D Navier-Stokes solver [4]. The cross sectional mesh (144x64 cells) used for the viscous calculations is compared to the (200x40 cells) mesh used in the conical calculations in **Fig. 16**. For the Navier-Stokes calculations the pressure side is discretized with fewer cells. Mesh clustering near the wall is visible on the right side of the figure.

Fig. 17 compares viscous and inviscid flow structures using iso Mach lines as well as streamlines. The laminar onflow conditions are set to M_∞=4; α=10°; Re=5000000 and a wall temperature of 888 Kelvin is used. The calculated aerodynamic coefficients are given in the figure's right side for the viscous calculation. Note that only the contributions of surface pressure are used here. The conical solution and the coefficients are shown on the left side. Both flow structures are very similar on both fine meshes. Viscous and inviscid calculations predict wing leading edge separation resulting in big primary and secondary vortices. The viscous solution shows a primary vortex having two centers and a stable secondary vortex. The conical fine solution (compare Fig. 12 and Fig. 13) is oscillating. It shows phases of the primary vortex core beeing split. The secondary vortex also oscillates. On the flattened body part both solutions predict another flat vortex. This vortex is generated by the adverse pressure gradient on the body. The gradient acts in addition to the total pressure losses yielded by the crossflow shock on top of the primary vortex at its inboard side. Although the underlaying separation mechanisms are different on both sides of the figure the resulting flow structures are in very good agreement. No vortex generating crossflow shocks near the surface (necessary in the conical Euler calculation) exist in the viscous flow solution. There is only one crossflow shock visible which terminates the outer expansion region. Because both flow structures are very similar it is not surprising that the calculated lift and drag coefficients differ less than 1%.

The viscous and inviscid flow structures at M_∞=6 are given in **Fig. 18.** The calculated flow structures are visualized using iso Mach lines and streamlines. The laminar Navier-Stokes solution predicts on the coarse mesh a leading edge separation with a single vortex while the conical solution (coarser mesh than in Fig. 17) gives the complicated shock structure with a flat separation bubble far inboard, compare Fig. 7 and Fig. 8. But despite differences concerning the separation the outer global flow structure is quite comparable and aerodynamic coefficients are in excellent agreement. The increased onflow Mach number changes the separated inviscid flow structure from leading edge separation to the type with separation bubble. In the viscous calculations the separation type seems not to change. Comparing the viscous flow structures of Fig. 17 and Fig. 18 shows that the coarser mesh at the higher onflow Mach number does not predict a secondary separation. Therefore the primary vortex has a closed shape with a single center. It is believed that a viscous flow solution on the fine mesh at M_∞=6; α=10° will show identical features of the lower Mach number case. On the other hand may the reduced mesh-inherent numerical dissipation drive the solution to become more similar to the flow structure of the conical solution on the left hand side of Fig. 18.

4.5 Conclusion

The conical Euler method is a fast and accurate design tool. It is best applicable to calculate aerodynamic coefficients and flow variable distributions of naturally attached flows especially on windward sides of forebodies. The use of this tool to calculate separated inviscid leeside flows is possible. The aerodynamic coefficients are shown to be accurate enough to be used in a spaceplane design cycle. However, the necessary effort to establish confidence in the separated inviscid flow structure is high. Mesh convergence checks have to be performed. They also serve to estimate the level of numerical error that influences the separated leeside flow structure. Accurate measurements are necessary to validate the proposed numerical tool for the calculation of shock-induced separated flows.

5. Summary

The present paper investigates the inviscid flow structure of a generic spaceplane forebody at two hypersonic Mach numbers. A conical upwind Euler Method is used to calculate aerodynamic coefficients and flow structures of a delta wing with blunt leading edges. The influence of discretization errors on the calculated conical leeside flow structures is addressed. Two types of inviscid separated vortical flow are

found and compared to viscous calculations. This enables to judge about the applicability of conical Euler methods as fast design tools for pointed spaceplane forebodies.

6.References

[1] Liou, M.-S.; Steffen, Ch.:
A New Flux Vector Splitting Scheme.
Journal of Computational Physics, Vol. 107, No. 1 pp. 23-39, 1993.

[2] Kroll, N.; Herrmann, U.; Radespiel, R.:
Discretization Properties in Hypersonic Flows.
DLR-IB 129-92/28, 1993.

[3] Van Leer, B.:
Flux-Vector Splitting for the Euler Equations.
Lecture Notes in Physics, Vol. 170, pp. 507-512, Springer Verlag, 1982.

[4] Kroll, N.; Radespiel, R.:
An improved Flux Vector Split Discretization Scheme for Viscous Flows.
DLR-FB 129-93/53, 1993.

[5] Ventkatakrishnan, V.:
On the Accuracy of Limiters and Convergence to Steady State Solutions.
AIAA 93-0880, 1993.

[6] Herrmann, U.:
IMESH - An Interactive Mesh Generation Package for Graphics Super Workstations.
3rd International Conference on Numerical Grid Generation in Computational Fluid Dynamics and related Fields, June 3-7, Barcelona, 1991.

[7] Findling, A.; Herrmann, U.:
Development of an Efficient and Robust Solver for Elliptic Grid Generation.
3rd International Conference on Numerical Grid Generation in Computational Fluid Dynamics and related Fields, June 3-7, Barcelona, 1991.

[8] Wardlaw, A.B.; Davis, S.F.:
Euler Solutions for Delta Wings.
AIAA 89-3398-CP, 1989.

[9] Pandolfi, M.; Larocca, F.:
Transonic Flow About a Circular Cylinder.
Computer & Fluids, Vol. 17, pp. 205-220, 1989.

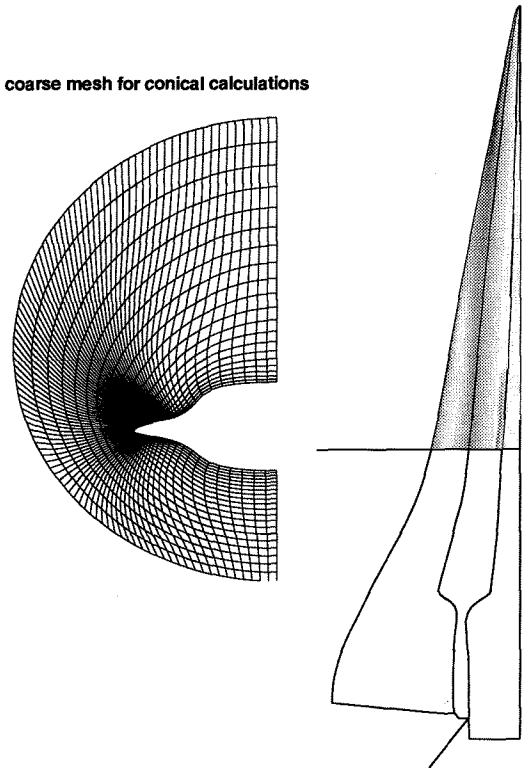

Fig. 1 Generic hypersonic spaceplane.

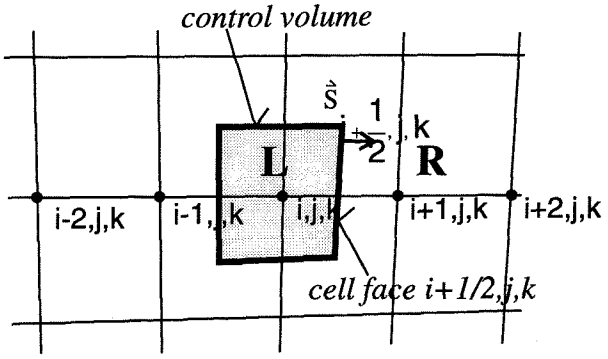

Fig. 2 Control volume for flux calculation.

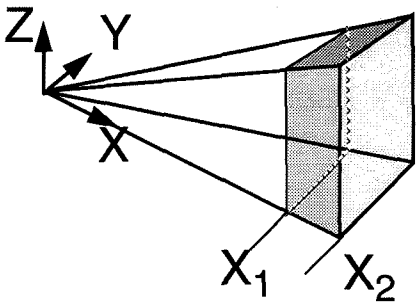

Fig. 3 Special control volume for conical flows.

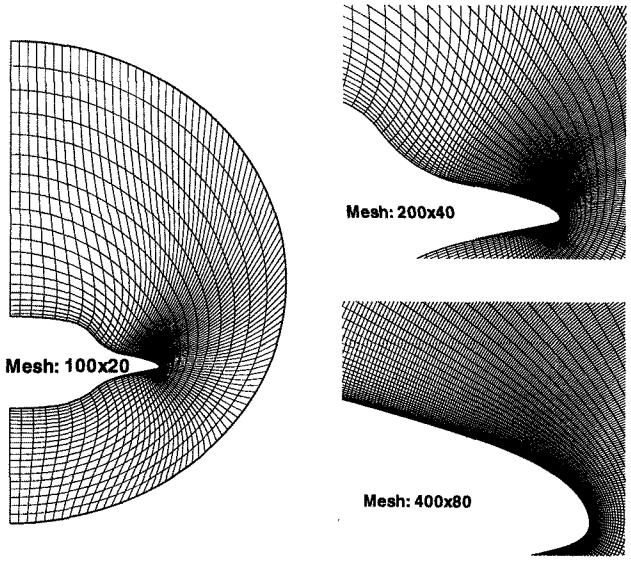

Fig. 4 Views of the used meshes.

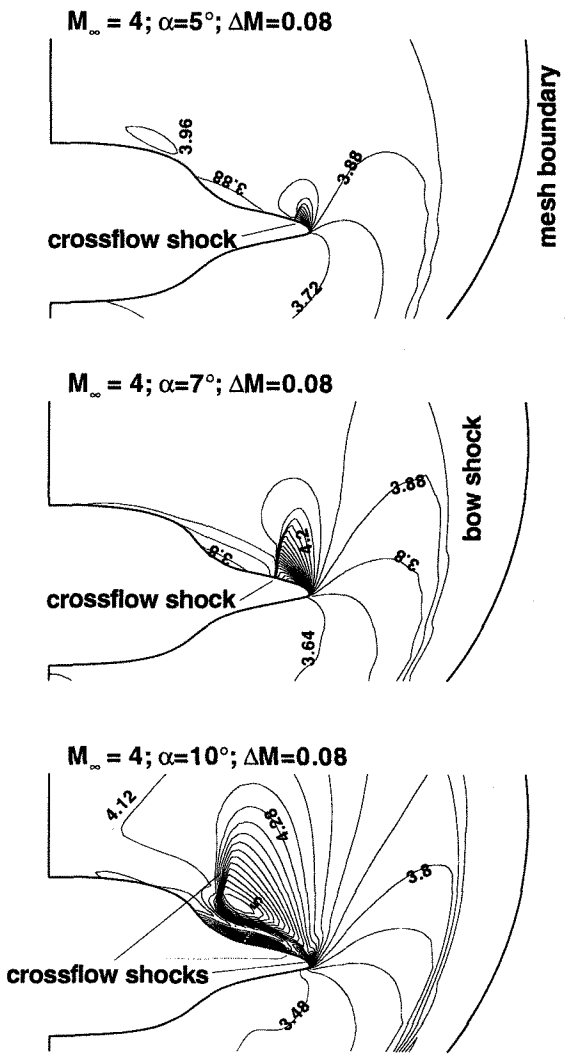

Fig. 5 Iso Machlines for three angles of attack on a 200x40 mesh; M_∞=4.

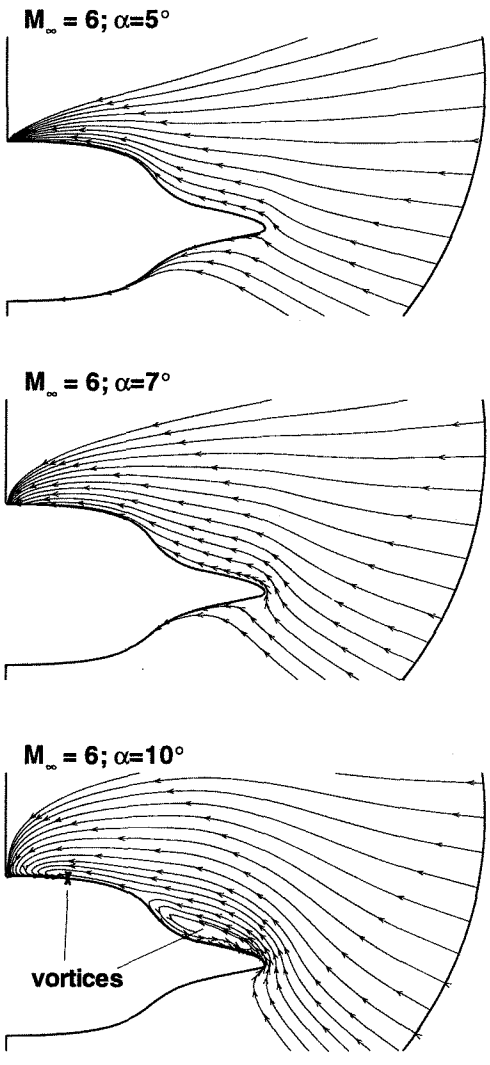

Fig. 6 Streamlines for three angles of attack on a 200x40 mesh; M_∞=4.

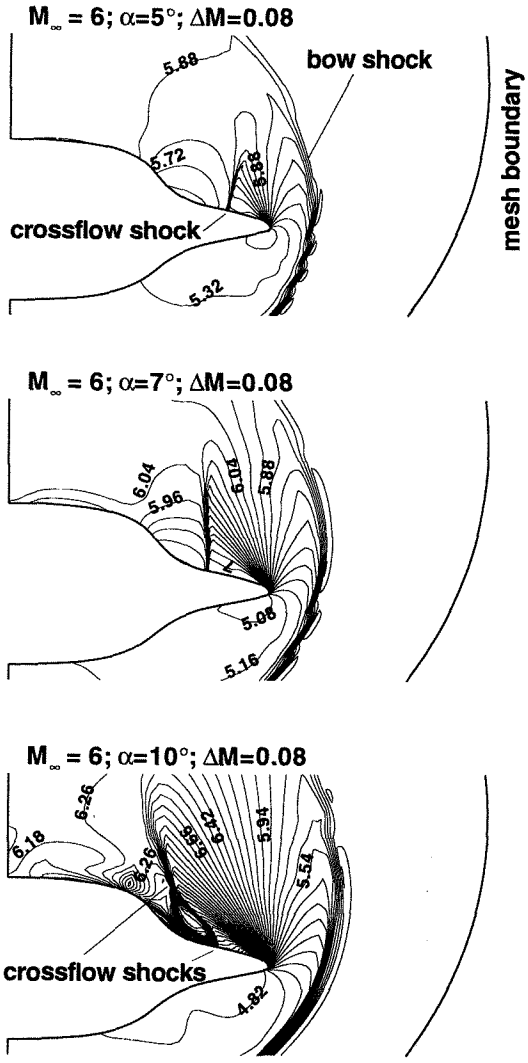

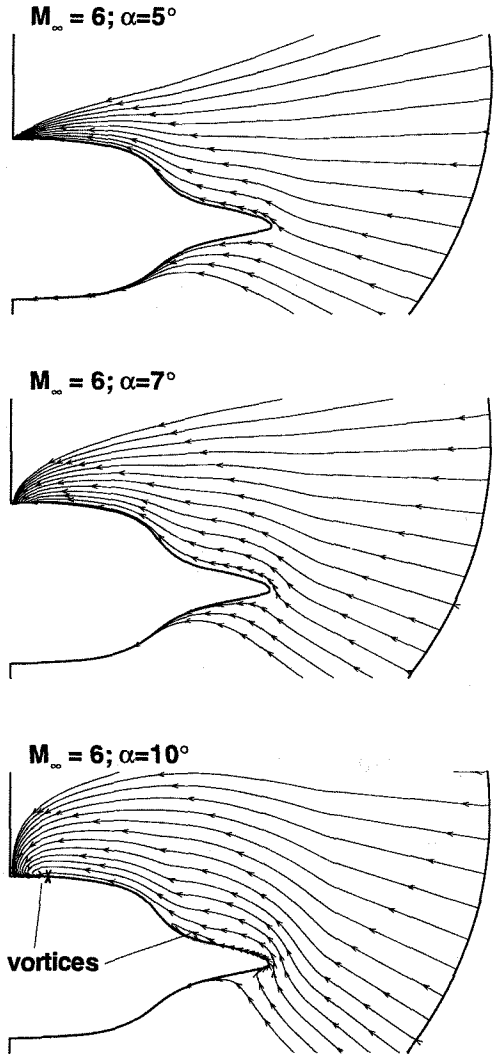

Fig. 7 Iso Machlines for three angles of attack on a 200x40 mesh; M_∞=6.

Fig. 8 Streamlines for three angles of attack on a 200x40 mesh; M_∞=6.

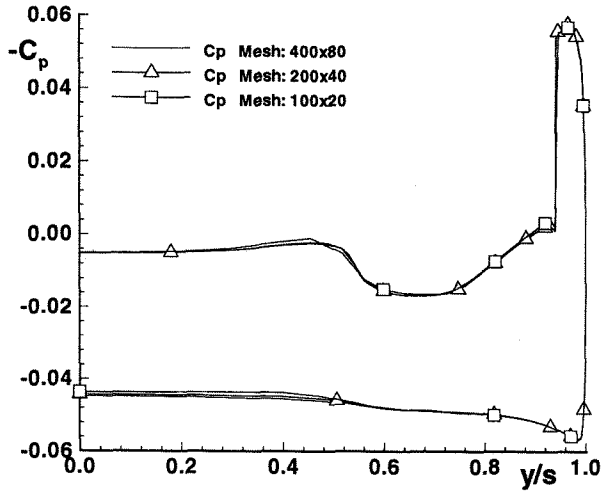

Fig. 9 C_p over delta wing span y/s at M_∞=4, α=5°.

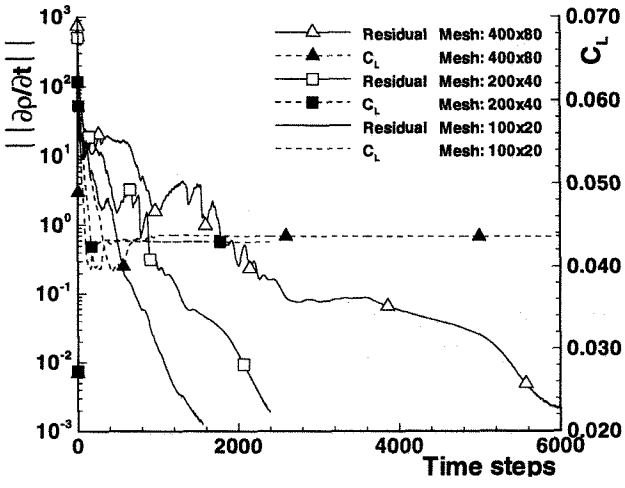

Fig. 10 Convergence for M_∞=4, α=5°.

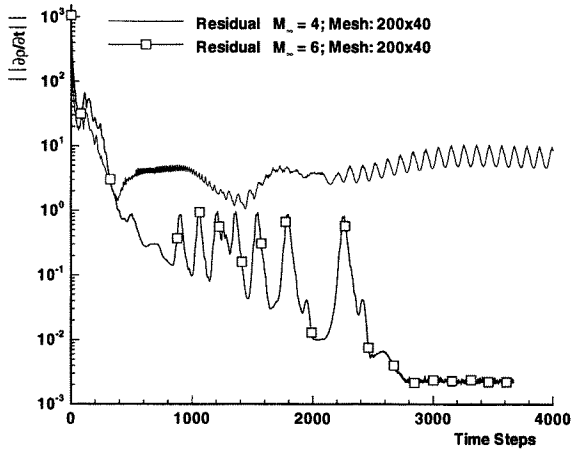

Fig. 11 Convergenz history for M_∞=4 and 6.

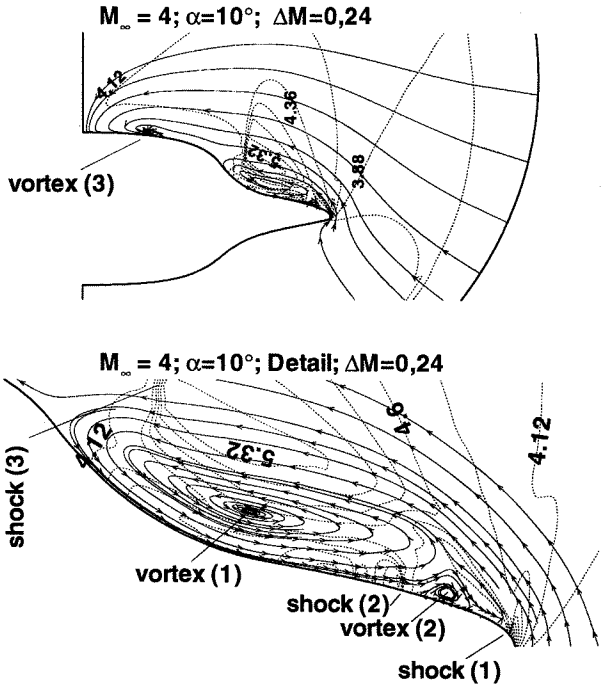

Fig. 12 Flow structure at M_∞=4; α=10° on the 400x80 mesh; low Residual.

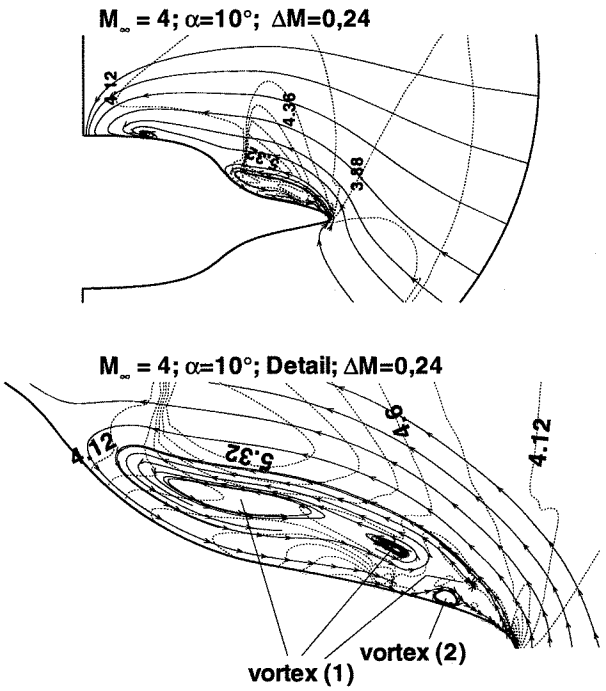

Fig. 13 Flow structure at M_∞=4; α=10° on the 400x80 mesh; high Residual.

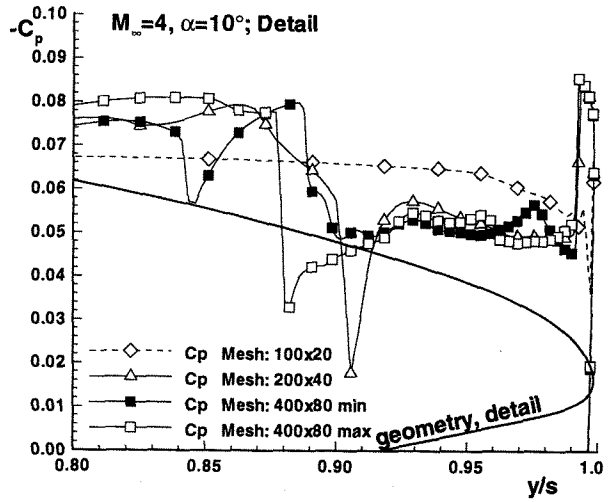

Fig. 14 C_p over delta wing span y/s, solutions with separation for M_∞=4.

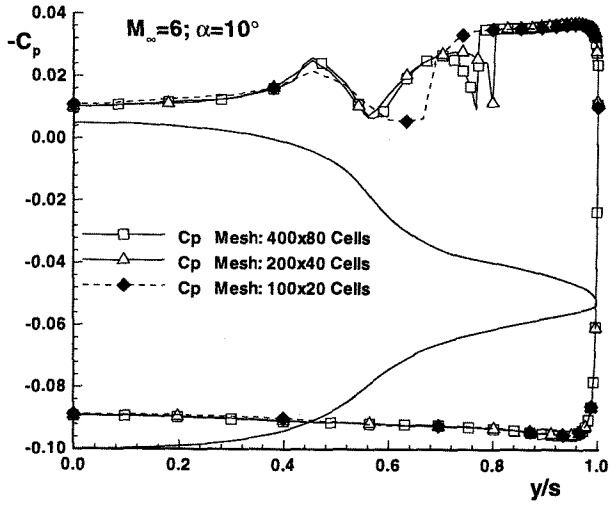

Fig. 15 C_p over delta wing span y/s, solutions with separation for M_∞=6.

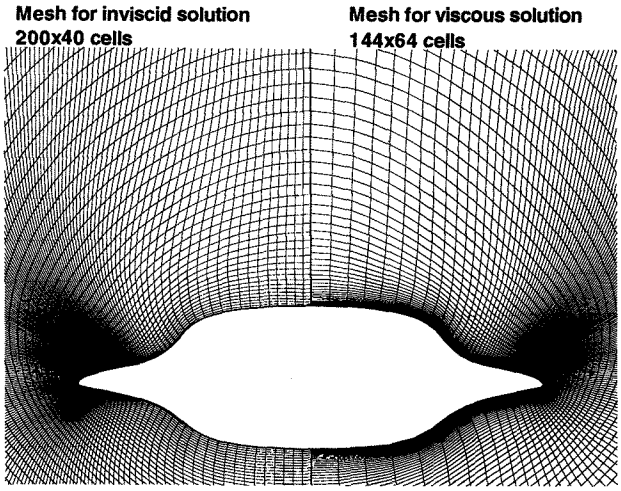

Fig. 16 Meshes used for inviscid conical and 3D viscous calculations.

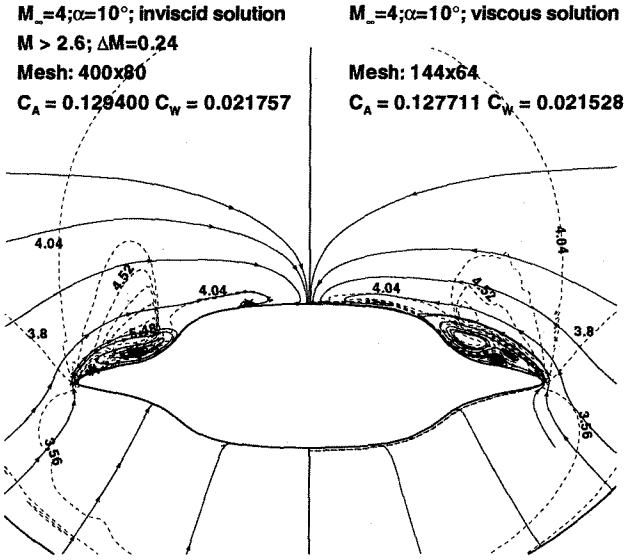

Fig. 17 Iso Mach and streamlines of viscous and inviscid solution; M_∞=4; α=10°.

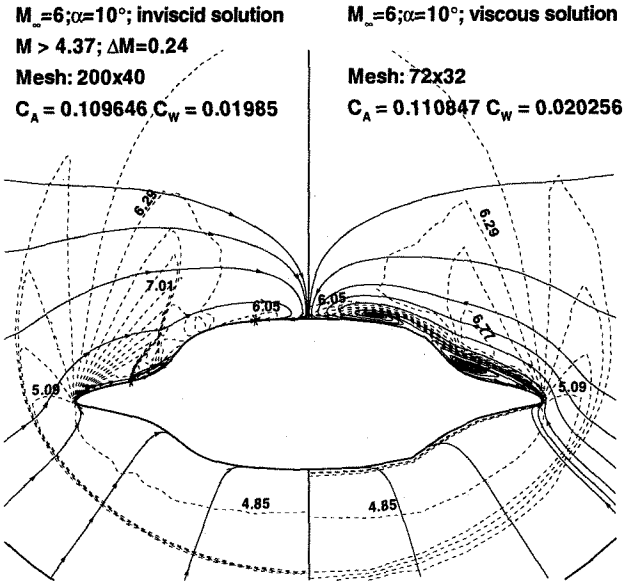

Fig. 18 Iso Mach and streamlines of viscous and inviscid solution; M_∞=6; α=10°.